Stochastic calibration of a carbon nitridation model from plasma wind tunnel experiments using a Bayesian formulation

Anabel del Val, Olivier Le Maitre, Pietro Marco Congedo, Thierry E. Magin

Stochastic calibration of a carbon nitridation model from plasma wind tunnel experiments using a Bayesian formulation

Anabel del Val[a,b,*], O. Le Maître[c], Pietro M. Congedo[b], Thierry E. Magin[a]

[a] *von Karman Institute for Fluid Dynamics, Chaussée de Waterloo 72, 1640 Rhode-St Genèse, Belgium*
[b] *Inria, Centre de Mathématiques Appliquées, École Polytechnique, IPP, Route de Saclay, 91128 Palaiseau Cedex, France*
[c] *CNRS, Centre de Mathématiques Appliquées, École Polytechnique, IPP, Route de Saclay, 91128 Palaiseau Cedex, France*

Abstract

In this work, we calibrate a carbon nitridation model for a broad span of surface temperatures from existing plasma wind tunnel measurements by accounting for experimental and parametric uncertainties. A chemical non-equilibrium stagnation line model is proposed to simulate the experiments and obtain recession rates and CN densities, the measured model outputs. First, we establish the influence of the experimental boundary conditions and nitridation parameters on the simulated observations through a sensitivity analysis. Results show that such quantities are mostly affected by the efficiency of nitridation reactions at the gas-surface interface. We then perform model calibrations for each experimental condition and compare them based on the experimental data used. This allows us to check the consistency of the experimental dataset. Using only the trustworthy experimental data, we perform a calibration of Arrhenius law parameters for nitridation efficiencies considering all available experimental conditions jointly, allowing us to compute nitridation efficiencies even for surface temperatures for which there are no reliable experimental data available. The stochastic Arrhenius law agrees well with most of the data in the literature. This result constitutes the first nitridation model extracted from plasma wind tunnel experiments with accurate uncertainty estimates.

Keywords: Thermal Protection Systems, Ablation, Uncertainty Quantification, Bayesian Inference

1. Introduction

Space vehicles entering dense planetary atmospheres must withstand extreme heating conditions to protect the astronauts and cargo from damage. Aerospace engineers must rely on selected materials and a robust design of the Thermal Protection System (TPS) to protect spacecraft from intense heat loads [1]. The interaction between chemically reacting gas and TPS is governed by the material behavior which injects new species into the boundary layer through different mechanisms [2]. In particular, we focus on ablative materials which, in addition to dissipating a significant amount of heat through radiation, dissipate the remaining heat by converting thermal energy into decomposition and degradation of the material itself, causing the surface of the ablative material to recess over time. Ablative TPS are generally constructed from rigid carbon fiber or silicon composites, impregnated with an organic resin matrix which serves as a pyrolyzing binder and provides strength to the overall TPS structure.

Characterizing ablation phenomena for different atmospheric and material compositions is quite challenging. It is important to understand the coupling mechanisms between material surface properties and the resulting ablation rates which in turn are coupled to the flowfield computations [3]. A key element of the modeling behind these phenomena is the surface chemical processes that are taken into account to explain the experiments. It is not always straightforward, from an a priori point of view, to know which chemical processes underpin the macroscopic effects we see in thermal protection materials subjected to reactive flow environments. Through dedicated experiments that manage to isolate and identify different chemical mechanisms, we are now in the position to fill in the knowledge of the selected model parameters with experimental data.

*Corresponding author: von Karman Institute for Fluid Dynamics, Chaussée de Waterloo 72, 1640 Rhode-St-Genèse, Belgium. *Email address:* ana.isabel.delvalbenitez@vki.ac.be (A. del Val)

Among them, the nitridation reaction $C_s + N \rightarrow CN + 0.34eV$ on a solid (s) carbon surface is still hard to predict accurately at temperatures above 1000 K. Even though the low exothermic energy of the nitridation reaction does not directly have a significant influence on the wall heating rate, it can indirectly affect recombination reactions at the wall that participate to the general heat balance. In the literature [4–10], there exist multiple experimental ways of testing for carbon nitridation efficiencies, from Inductively-Coupled Plasma (ICP) wind tunnels to molecular beams. Not a single experiment has a straightforward interpretation for the derivation of nitridation efficiencies. They require several layers of assumptions about the experimental apparatus and its theoretical modeling that could render the obtained parameters dubious. Furthermore, the different methods used to rebuild nitridation efficiencies from experimental data give out results that differ by several orders of magnitude with no account of uncertainties. Among such rebuilding methods, there is only one stochastic approach proposed in the work of Upadhyay et al. [11]. In their contribution, the authors re-formulated the inference problem performed by Zhang et al. [7] as a statistical inverse problem, which they solved using the Bayesian formalism. They formulated four different model classes that differed in the physical model itself and the parameters considered uncertain. They were able to calibrate power laws for each model class for the dependence of nitridation reaction efficiencies with surface temperatures. Even though this pioneering work represents a step in the good direction to tackle learning nitrogen ablation parameters from data, the physical models used were built on several simplifying assumptions and the nitrogen wall concentration was estimated without taking into account nitridation reactions. Moreover, the final calibrated power laws spanning a range of wall temperatures did not capture any of the additional nitridation data reported in the literature.

In recent works, Helber et al. [12] determined nitridation reaction efficiencies of graphite at surface temperatures up to 2,575 K by using a coupled deterministic experimental-numerical approach. For the reconstruction of nitridation efficiency parameters, they used recession rate measurements, while assuming negligible the recombination of nitrogen at the wall. The authors pushed the boundaries of the state of the art with respect to the work of Suzuki et al. [6] for higher surface temperatures. They did so by including nitridation in the computation of atomic nitrogen wall concentration as well as adding optical emission spectroscopy measurements of the CN radiative signature in the flowfield in front of the graphite sample. The more accurate modeling, together with an additional independent measurement sensitive to CN production allowed them to compute an updated Arrhenius law for nitridation reaction efficiencies backed-up by the spectroscopy measurements. Helber et al. performed their analyses assuming conventional error bars in the measurements as well as linear behavior of the model-predicted recession rates with nitridation reaction efficiencies, in such a way that lower and upper bounds of the nitridation parameters were directly traced to upper and lower bounds of the measured recession rates. This ad-hoc treatment of the stochastic nature of the data together with the implications of the assumptions made for the analysis could have potentially biased the results and altered the conclusions that ensued. Furthermore, no estimation of the confidence on the nitridation model was derived as a result.

In the present work, we exploit Helber et al.'s experimental data for the purpose of inferring a nitridation reaction efficiency model in a rigorous statistical setting by means of a Bayesian approach. While classical inverse approaches commonly used in the reviewed literature are ill-equipped to produce reliable model calibrations and validations, stochastic inverse approaches include modeled uncertainty along with the physical problem of interest [13]. As a result, we are able to accurately and objectively quantify the uncertainty affecting nitridation reaction efficiencies for different surface temperatures. The methodology is as follows. We first conduct an a priori analysis of the forward model, a chemical non-equilibrium stagnation line flow model with nitridation as the only surface mechanism. We can assess the sensitivity of the model to each input parameter by propagating a priori uncertainty ranges. The input parameters constitute the boundary conditions of the experiments and the model parameters concerning nitridation. To lighten the computational burden of the propagation, we construct different Gaussian Process (GP) surrogates for the model outputs. This a priori exploration of the model leads to the simplification of the inference problem by prescribing the important experimental observations for nitridation efficiencies determination. Measurements of material recession rates and local CN mass densities are used, together with static pressures, dynamic pressures and wall temperatures, to infer all parameters needed to define the flow solutions, where we include the nitridation reaction efficiencies. When used independently, measured recession rates and CN densities each give information about nitridation reactions. As they are both part of the same experiments, one model should be capable of explaining both observations at once. Checking for this consistency with the available data has the potential of improving the characterization of nitridation mechanisms and signaling issues with the model and/or the experiments. We make use of the surrogate models built previously for the sensitivity analysis to make the problem of the inference computation-

ally efficient when sampling the posterior distribution. Further, an additional original contribution of this work is to combine all available measurements for the calibration of a stochastic Arrhenius law, extending the computation of nitridation efficiencies to a broader span of surface temperatures for which there are no reliable experimental data. In sum, this work aims at developing a predictive model for carbon nitridation with accurately defined uncertainty estimates. Furthermore, the different steps taken to achieve such results offer insights about the important physical processes that drive the material ablation under the considered flow conditions which could not be produced using simpler deterministic approaches.

The article is organized as follows. Sec. 2 addresses the theoretical models, numerical methods and experimental data used in this work. Sec. 3 introduces the inference methodology in detail. Sec. 4 shows and discusses the obtained results of this work. Sec. 5 presents the conclusions and outlook.

2. Nitridation experiments, modeling and simulations

In this section we recall the experiments, models and methods used for this work. First, we discuss the experimental facility and methods used to obtain the experimental data. We then focus on the theoretical and numerical simulations of the measured quantities from which we want to infer nitridation efficiencies.

2.1. Experiments

The experimental scenario is depicted in much detail in [12]. In this section, we briefly describe the measurements and their associated uncertainties.

The experiments were performed to rebuild nitridation reaction efficiencies γ_N^{CN} for graphite at high surface temperatures. For this, Helber et al. [12] experimentally observed the response of graphite samples to a subsonic plasma flow produced by the von Karman Institute's (VKI) Plasmatron facility (see Fig. 1). This process creates a reacting boundary layer around the exposed sample where species resulting from the ablation reactions are injected. Overall, Helber et al. were interested in measuring the rate of recession of the graphite sample due to the ablation reaction $C_s + N \rightarrow CN$, as well as the radiation signature from the CN molecule injected in the boundary layer. Both measurements contain information about the nitridation process. Operating conditions of the VKI Plasmatron were carefully chosen to be of high power, high heat fluxes, producing high surface temperatures. High heating helps dissociating the molecular nitrogen, creating a higher concentration of atomic nitrogen which enables more nitridation activity at the wall. The high surface temperatures play the same role in promoting nitridation reactions at the wall, enhancing the phenomenon we want to observe.

Apart from the dedicated nitridation measurements, Helber et al. performed another set of tests aimed at recovering the free stream conditions for each case by using a water-cooled copper calorimeter [12]. In this work, we evaluate quantitatively how important is the information about the free stream conditions in the inference of γ_N^{CN}. For this purpose, we only depict here the additional pressure measurements that are a priori included in the inference proposed. A water-cooled Pitot probe measured the dynamic pressure P_d within the plasma jet, and an absolute pressure transducer recorded the static pressure P_s in the Plasmatron chamber.

All the different probes and test sample holders were exposed sequentially to the same plasma flow and the nitridation measurements were recorded until steady-state was maintained for 300 s. The following tables summarize the different measurements and uncertainties used in this work. In Table 1 the measured quantities are the dynamic pressure P_d, the wall temperature T_w, the chamber static pressure P_s, the recession rate $\dot{s}$ and the local CN densities ρ_{CN} estimated from spectra measurements locally resolved.

Table 1: Experimental data.

Experiment ID	P_d [Pa]	T_w [K]	P_s [Pa]	$\dot{s}$ [μm/s]	ρ_{CN} [μg/m^3]
G4	231	2225	1500	1.41	385
G5	268	2410	1500	1.64	800
G6	312	2535	1500	2.60	1850
G7	330	2575	1500	2.51	1050

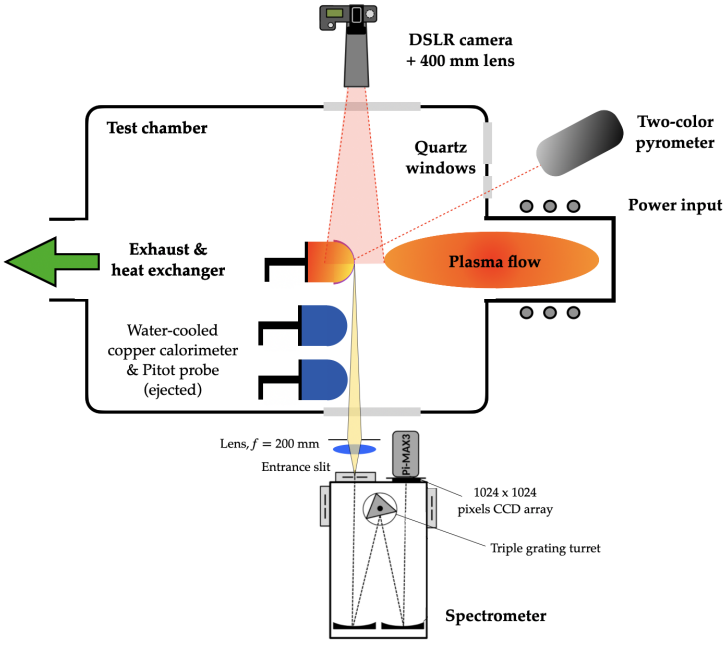

Figure 1: Schematic view of the ablation experimental set-up for the Plasmatron facility. Figure adapted from Helber [14]

The experimental uncertainties are assumed independently distributed Gaussian distributions $\mathcal{N}(\mu, \sigma)$ with σ taken considering the bounds given on the measurements as 2σ level of confidence [14–16].

Table 2: Experimental uncertainties.

Experiment ID	P_d [Pa]	T_w [K]	P_s [Pa]	$\dot{s}$ [μm/s]	ρ_CN [μg/m^3]
G4	$\mathcal{N}(231, 2.31)$	$\mathcal{N}(2225, 11.12)$	$\mathcal{N}(1500, 22.5)$	$\mathcal{N}(1.41, 0.26)$	$\mathcal{N}(385, 52)$
G5	$\mathcal{N}(268, 2.68)$	$\mathcal{N}(2410, 12.05)$	$\mathcal{N}(1500, 22.5)$	$\mathcal{N}(1.64, 0.27)$	$\mathcal{N}(800, 100)$
G6	$\mathcal{N}(312, 3.12)$	$\mathcal{N}(2535, 12.67)$	$\mathcal{N}(1500, 22.5)$	$\mathcal{N}(2.60, 0.27)$	$\mathcal{N}(1850, 250)$
G7	$\mathcal{N}(330, 3.3)$	$\mathcal{N}(2575, 12.87)$	$\mathcal{N}(1500, 22.5)$	$\mathcal{N}(2.51, 0.25)$	$\mathcal{N}(1050, 162)$

2.2. Theoretical models and simulations

We use a one dimensional form of the full Navier-Stokes equations in order to perform efficient simulations of a high temperature, reacting flow with complex physico-chemical models and boundary conditions. Originally proposed in [17], this formulation is called "Dimensionally Reduced Navier-Stokes Equations (DRNSE)" and, in the present study, it is implemented in an in-house software developed by Munafò [18]. This code is able to reproduce the flow along the stagnation-line of spherical and cylindrical bodies. The system is dimensionally reduced by means of the stagnation-line theory for axisymmetric problems: the system of equations is firstly transformed in spherical (r, θ, ϕ) coordinates, while exploiting the axisymmetry around the r axis with $u_\phi = \partial/\partial\phi = 0$. Applying separation of variables and allowing θ to tend to zero reduces the problem to one dimension; further details can be found in [17].

In the solver, the spatial discretization is performed by means of a cell-centered finite volume method. The numerical advective fluxes are computed by means of the AUSM$^+$-up2 scheme [19], which splits the flux into a convective and a pressure terms. Second order accuracy in space is achieved by using an upwind reconstruction to obtain the cell interface variables. The diffusive fluxes and source terms are both evaluated in terms of primitive variables: ρ_i, u, v, T . The value of the primitive variables and their gradients at the volume interface are computed by a weighted average and a central finite difference approximation, respectively. The cell center value of the primitive variables to be used

in the evaluation of the diffusive source terms are computed using a two-point central finite-difference approximation. A fully implicit scheme is used for the present study. The code is coupled with the Mutation^{++} library [20]. Species thermodynamic properties are obtained from Rigid-Rotor Harmonic-Oscillator computations, and relative mixture quantities are derived from pure species quantities. The transport properties are derived from kinetic theory, which provides relationships for macroscopic transport coefficients based on microscopic collision integrals. The chemical production rates for species, based on elementary chemical reactions, including third body, are calculated by taking the forward reaction rate coefficients specified by the user in an Arrhenius law form. The backward rate coefficient is determined by satisfying the equilibrium relation. The library has been designed, implemented and extensively tested to ensure high-fidelity together with low computational costs.

A coupled ablative boundary condition is also included in a generalized formulation [21] in Mutation^{++} based on surface mass and energy balances. Several other authors have applied this approach to study the ablative and non-ablative gas-surface interaction of thermal protection materials with the surrounding flowfield [22–24]. The advective and the diffusive fluxes at the gas-surface interface are obtained by solving the surface species mass balance. This balance is obtained limiting the control volume of the mass conservation equation to the thin lamina representing the gas-surface interface [12]. In this study, we do not need to include a surface energy balance given that the temperature at the wall T_w is measured and imposed.

The inlet boundary condition used for the simulations of such reacting flows comprises species densities ρ_i, temperature T, and velocity components u, v, while the surface conditions are temperature at the wall T_w, which closes the energy equation; we assume no slip condition, which closes the momentum equations, and we define surface mass balances for the species mass equations. These mass balances need the chemical mechanism at the surface to be specified and we also need to give values to the different parameters. The information needed to prescribe the boundary condition at the free stream pertains to a supersonic inlet even though we want to carry out subsonic simulations. This methodology has been investigated and discussed in [25], where it was verified that the solution of the Riemann problem at the boundary interface automatically screens the information needed from the inlet.

All in all, we intend to find the flow solutions that are compatible with our experimental observations under the considered model. This means that from the observations reported by Helber et al. [12], we want to infer the inlet conditions and the wall conditions in such a way that we are left with a population of possible flow solutions. As we work with a mixture of 9 species: $\mathcal{S} = \{\mathrm{e^-}, \mathrm{C^+}, \mathrm{C_2}, \mathrm{C_3}, \mathrm{CN}, \mathrm{C}, \mathrm{N}, \mathrm{N^+}, \mathrm{N_2}\}$, we are left with a 14-dimensional problem if we only consider nitridation at the wall. The predictive quantities $\dot{s}$ and ρ_CN we are after would read

$$\dot{s} = \dot{s}\left(\rho_{\delta,i}, u_\delta, v_\delta, T_\delta, P_\delta, T_\mathrm{w}, \gamma_\mathrm{N}^\mathrm{CN}\right) \quad \forall i \in \mathcal{N}_\mathrm{s}, \tag{1}$$

$$\rho_\mathrm{CN} = \rho_\mathrm{CN}\left(\rho_{\delta,i}, u_\delta, v_\delta, T_\delta, P_\delta, T_\mathrm{w}, \gamma_\mathrm{N}^\mathrm{CN}\right) \quad \forall i \in \mathcal{N}_\mathrm{s}, \tag{2}$$

where the subscript δ defines the boundary layer edge conditions. The terms u_δ and v_δ refer to the radial and axial stagnation line velocities, respectively. The number of species included in the mixture is denoted by $\mathcal{N}_\mathrm{s}$. The fact that we carry out one dimensional simulations and we need to specify two velocity components falls from the assumed ansatz for the derivation of the dimensionally-reduced Navier-Stokes equations [17]. The velocity components should be set to comply with the velocity gradient and dynamic pressure we want to impose at the inlet. As can be appreciated, not all the unknown parameters are of interest for us given that we are only interested in learning the nitridation parameter $\gamma_\mathrm{N}^\mathrm{CN}$. Nevertheless, these nuisance parameters must be included in the inference as they constitute unknowns of the problem and they are needed to carry out the flow simulations.

We can reduce the dimensionality of the problem by taking into account some physical relationships from which we can recuperate some boundary layer edge parameters. The subsonic VKI Plasmatron flowfield, composed by the torch and test chamber, is numerically simulated using an axisymmetric Local Thermodynamic Equilibrium (LTE) magnetohydrodynamics solver which computes the solution of the Navier-Stokes equations coupled to the Maxwell's equations under certain assumptions (VKI ICP code [26–28]). Initially developed as a standalone tool, the VKI ICP code is nowadays integrated into the Computational Object-Oriented Library for Fluid Dynamics (COOLFluiD) [29]. The ICP simulation takes the inlet mass flow $\dot{m}$, the power transmitted to the plasma from the coils P_plasma, the chamber static pressure P_s and the probe geometry as inputs. The power transmitted to the plasma flow is a percentage of the total power injected to the coils P_el. This percentage is usually taken as 50% [30]. From such subsonic flowfield

simulations we can derive non-dimensional parameters (NDPs) for the boundary layer thickness δ, the velocity gradient, and the axial gradient of the velocity gradient, both at location δ [30, 31]. The dynamic pressure, corrected for viscous effects $P_\mathrm{d}/K_\mathrm{H} = 1/2\rho_\delta v_\delta^2$ with K_H as Homman's correction factor [32], is used as a convenient proxy for the axial velocity v_δ. Together, the non-dimensional parameters and the dynamic pressure define the inlet velocities imposed by the experimental conditions. The radial velocity u_δ can be expressed as a linear relationship with v_δ through the velocity gradient $(\partial u/\partial x)\Big|_\delta = (u_\delta + v_\delta)/R_0$ [18], where x is the spatial coordinate for the radial direction and R_0 is the equivalent spherical radius of the probe. As we are assuming a boundary layer edge in chemical equilibrium, the density ρ_δ in the dynamic pressure expression, as well as species mass densities $\rho_{\delta,i}$ are defined by the temperature T_δ and pressure P_δ for a fixed elemental composition. In sum, the following functional relationships are introduced as valid additional relations of the boundary layer edge conditions to some characteristics of the experimental set-up

$$\rho_{\delta,i} = \rho_{\delta,i}(T_\delta, P_\delta), \tag{3}$$

$$u_\delta = u_\delta\left(\mathrm{NDPs}, P_\mathrm{d}, T_\delta, P_\delta\right), \tag{4}$$

$$v_\delta = v_\delta\left(\mathrm{NDPs}, P_\mathrm{d}, T_\delta, P_\delta\right). \tag{5}$$

It is possible to test these assumptions by getting rid of the additional structure in our model, considering species densities and different thermal bath temperatures as unknowns of the inference problem. At the end of the analysis, for given Plasmatron operating conditions, we are left with the expressions

$$\dot{s} = \dot{s}\left(P_\delta, T_\delta, P_\mathrm{d}, T_\mathrm{w}, \gamma_\mathrm{N}^\mathrm{CN}\right), \tag{6}$$

$$\rho_\mathrm{CN} = \rho_\mathrm{CN}\left(P_\delta, T_\delta, P_\mathrm{d}, T_\mathrm{w}, \gamma_\mathrm{N}^\mathrm{CN}\right), \tag{7}$$

where the momentum boundary layer edge parameters u_δ, v_δ have been replaced by the dynamic pressure P_d, given that the non-dimensional parameters are taken as constants [15]. These expressions constitute the dependencies of the forward model.

3. Stochastic calibration methodology

This section explores the different dependencies of the forward model and builds a hierarchy of influential parameters on the predictive quantities. This helps us understand what parameters are the drivers of the inference and what observations are relevant to consider. To do so, we first introduce the choice of surrogate models for the predictive quantities to make the process more efficient. We then derive the Bayesian framework for this problem by prescribing a likelihood function and prior distributions.

3.1. A priori analysis of the forward model

The forward model depicted in Sec. 2.2 depends on a set of nuisance parameters and quantities of interest. We are concerned with the capabilities of learning $\gamma_\mathrm{N}^\mathrm{CN}$ from the experimental data of Helber et al. For this purpose, we first perform an uncertainty propagation by assuming a priori uncertainty ranges on the input parameters. We then carry out a variance-based sensitivity analysis and derive sensitivity indices for the dependencies of the model. As already mentioned in Sec. 2.2, we do not take into account an additional set of experimental data collected to infer the free stream conditions of the flow for each case. This a priori analysis allows us to explore this choice and decide if that experimental data should be included in our analysis to enhance our learning capabilities of $\gamma_\mathrm{N}^\mathrm{CN}$.

Non-intrusive uncertainty propagation involves multiple evaluations of the forward model. This step can be very expensive and burdensome as each individual evaluation should also have good convergence properties. We decide to lighten the burden by building surrogates on the predictive quantities $\dot{s}$ and ρ_CN. These surrogate models are also used later in the inference.

3.1.1. Surrogate modeling

To construct the surrogates, we first introduce new canonical random variables for the 5 parameters upon which $\dot{s}$ and ρ_{CN} depend, $\boldsymbol{\xi} = (\xi_{P_\delta}, \xi_{T_\delta}, \xi_{P_\mathrm{d}}, \xi_{T_\mathrm{w}}, \xi_{\gamma_\mathrm{N}^{\mathrm{CN}}})$. We set $\boldsymbol{\xi}$ to be defined over the unit hypercube: $\boldsymbol{\xi} \in [0,1]^5$ in order to simplify the training and use of the surrogate models. We then fix the a priori ranges in the physical variables to be $P_\delta(\xi_{P_\delta}) = 1200 + \xi_{P_\delta} 500$, $T_\delta(\xi_{T_\delta}) = 9000 + \xi_{T_\delta} 4000$, $P_\mathrm{d}(\xi_{P_\mathrm{d}}) = 200 + \xi_{P_\mathrm{d}} 160$, $T_\mathrm{w}(\xi_{T_\mathrm{w}}) = 2000 + \xi_{T_\mathrm{w}} 2000$, and $\gamma_\mathrm{N}^{\mathrm{CN}}(\xi_{\gamma_\mathrm{N}^{\mathrm{CN}}}) = 10^{-4\xi_{\gamma_\mathrm{N}^{\mathrm{CN}}}}$, such that they all have canonical range 1. The ranges are chosen large enough to acommodate possible parameter values under the experimental conditions considered.

We seek to construct surrogates of the $\dot{s}$ and ρ_{CN} with this parametrization. In particular, we decide to proceed with the log of $\dot{s}$ and ρ_{CN} (from now on referred to as log variables) instead of the natural variables as it ensures the positivity of the approximation. More precisely, we aim for surrogate models of $Y_{\dot{s}}(\boldsymbol{\xi})$ and $Y_{\rho_{\mathrm{CN}}}(\boldsymbol{\xi})$ defined by

$$Y_{\dot{s}}(\boldsymbol{\xi}) \doteq \log\left(\dot{s}(\boldsymbol{\xi})\right), \tag{8}$$

$$Y_{\rho_{\mathrm{CN}}}(\boldsymbol{\xi}) \doteq \log\left(\rho_{\mathrm{CN}}(\boldsymbol{\xi})\right). \tag{9}$$

We propose to use Gaussian Process (GP) models to approximate these functions. GP models have been widely used in uncertainty propagation, sensitivity analysis, optimization and inverse problems [33]. Due to their statistical nature, a GP provides a measure of the uncertainty (variance) in the prediction. A more complete account on the training and use of GP models can be found in [13].

The surrogate models are built on an initial 600 points grid where Latin Hypercube Sampling (LHS) is chosen due to its capability to explore all the unit hypercube evenly. This is particularly important when dealing with chemical parameters such as $\gamma_\mathrm{N}^{\mathrm{CN}}$ which generally can cause irregular behavior of the simulated quantities, especially if the surface temperature T_w can also vary from point to point. An extra 600 points are added in a Monte Carlo fashion to enrich the approximation around the areas with largest variance of the GP prediction if needed. Fig. 2 shows the normalized L_2 norms of the errors of the surrogate approximations for both log variables. The L_2 norms are changing as we increase the number of points used to train the surrogates while keeping the same validation sets to compute the errors (10% of all available points). This process is done 1,000 times with different validation sets to produce the 95% confidence intervals depicted in Fig. 2. The normalized errors drop fairly quickly below 1%.

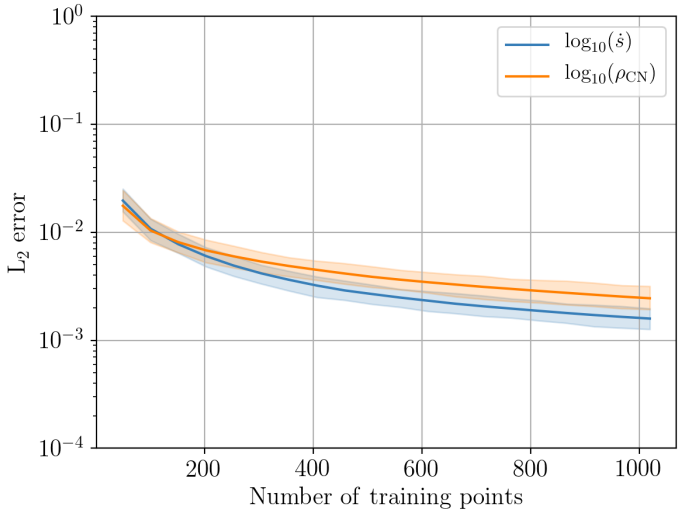

Figure 2: Normalized L_2-error norms of the log variables approximations.

3.1.2. Sensitivity analysis

Once we have built the surrogate models, we can propagate the uncertainty from the inputs and model parameters to the outputs. Particularly, we are interested in knowing if the uncertainty on the free stream information T_δ is

important for the variability of recession rates $\dot{s}$ and CN densities ρ_{CN}. If those two observed quantities are not sensitive enough to the variation of temperature T_δ, we would not need to add the additional experimental data to our inference as it would not bring any useful information for $\gamma_{\mathrm{N}}^{\mathrm{CN}}$. Furthermore, the treatment of the measurements for free stream determination entails additional models and computations, increasing the complexity of the inference for no gain.

We propagate the input distributions depicted in Table 3. In this case, we only perform this analysis for one of the experimental cases as the modeling and experimental data remain consistent for all. Whenever possible, the ranges and distributions of the input variables are taken directly from the available measurements. When no experimental counterpart is available, the same ranges as the ones prescribed for the construction of the surrogates are used. This is the case for the boundary layer edge temperature T_δ and the nitridation reaction efficiency $\gamma_{\mathrm{N}}^{\mathrm{CN}}$. The pressure at the edge of the boundary layer P_δ is taken as the chamber static pressure P_{s}, therefore its uncertainty is defined as the corresponding experimental uncertainty associated with P_{s}.

Table 3: Input uncertainties for the a priori forward model analysis.

Experiment ID	P_δ [Pa]	T_δ [K]	P_{d} [Pa]	T_{w} [K]	$\gamma_{\mathrm{N}}^{\mathrm{CN}}$
G5	$\mathcal{N}(1500, 22.5)$	$\mathcal{U}[9000, 13000]$	$\mathcal{N}(268, 2.68)$	$\mathcal{N}(2410, 12.05)$	$\log \mathcal{U}[-4, 0]$

The values in the table are normalized within the ranges prescribed for building the surrogates. We then obtain the corresponding uncertainty distributions for the canonical variables $\boldsymbol{\xi}$ from which to input the GP surrogate models and perform the propagation. Fig. 3 shows the values of $\dot{s}$ and ρ_{CN} for the propagated canonical inputs $\boldsymbol{\xi}$. This exercise clearly shows which parameter dominates the variability of each predicted quantity $\dot{s}$ and ρ_{CN}. Under the considered testing conditions (and also for the other test cases), $\gamma_{\mathrm{N}}^{\mathrm{CN}}$ is the most important parameter for the variability of recession rates and CN densities. None of the other parameters play a substantial role. We can appreciate a small influence of T_δ on the variability of ρ_{CN} but qualitatively seems very negligible compared to the effect of $\gamma_{\mathrm{N}}^{\mathrm{CN}}$.

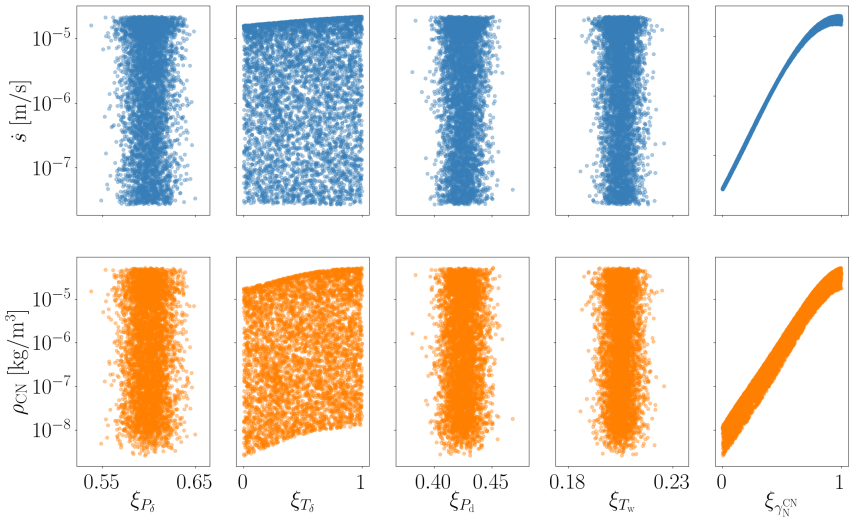

Figure 3: Resulting recession rates and CN densities for the propagated a priori uncertainty distributions of the canonical variables $\boldsymbol{\xi}$.

Quantitatively, we can compute the associated first and total order Sobol' indices [34] to establish a hierarchy among the variables and reliably assess the influence of the uncertainty of T_δ on $\dot{s}$ and ρ_{CN}. Fig. 4 shows the outcome of the Sobol' indices computation. The result encompasses almost two orders of magnitude difference in the influence of the uncertainty of $\gamma_{\mathrm{N}}^{\mathrm{CN}}$ over the uncertainty of T_δ on ρ_{CN} and even more for $\dot{s}$. This highlights the fact that good

knowledge of the boundary layer edge conditions does not play a significant role in the inference of $\gamma_{\mathrm{N}}^{\mathrm{CN}}$ from recession rates and/or CN densities when the other variables are known to the prescribed degree of uncertainty. We can now safely ignore the rest of the experimental data gathered by Helber et al. (no depicted in this work, see [12]).

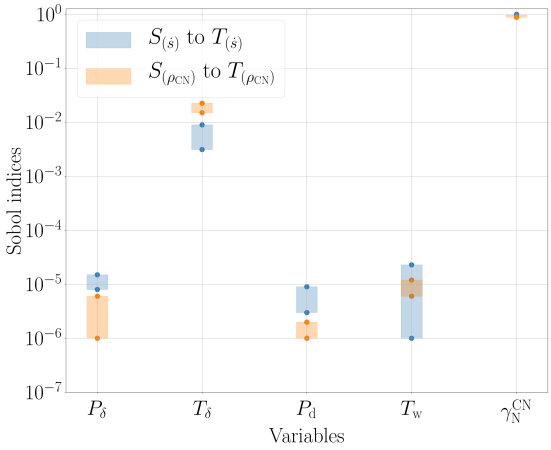

Figure 4: First and total order partial variance decompositions for $\dot{s}$ and ρ_{CN}. The rectangles represent the change from first to total order sensitivity indices.

3.2. Bayesian inference: likelihood function and prior distributions

The inference of model parameters uses the Bayes formula which can be generically formulated as

$$\mathcal{P}(\boldsymbol{q}|\boldsymbol{y}_{\mathrm{obs}}) = \frac{\mathcal{P}(\boldsymbol{y}_{\mathrm{obs}}|\boldsymbol{q})\,\mathcal{P}(\boldsymbol{q})}{\int_{\Omega}\mathcal{P}(\boldsymbol{y}_{\mathrm{obs}}|\boldsymbol{q})\,\mathcal{P}(\boldsymbol{q})d\boldsymbol{q}}, \tag{10}$$

where $\boldsymbol{q} = (P_\delta, T_\delta, P_{\mathrm{d}}, T_{\mathrm{w}}, \gamma_{\mathrm{N}}^{\mathrm{CN}})$ is the generic vector of parameters, having for components the parameters of the analysis. The vector $\boldsymbol{q}$ results from the stagnation line modeling and physical considerations presented in Sec. 2.2. The term $\boldsymbol{y}_{\mathrm{obs}} = (P_{\mathrm{d}}^{\mathrm{meas}}, P_{\mathrm{s}}^{\mathrm{meas}}, T_{\mathrm{w}}^{\mathrm{meas}}, \dot{s}^{\mathrm{meas}}, \rho_{\mathrm{CN}}^{\mathrm{meas}})$ is the vector of the measured quantities used for the analysis. For compact notation, we split the observations and parameters to be inferred in two distinct subsets. The subset $\boldsymbol{q}' = (P_\delta, P_{\mathrm{d}}, T_{\mathrm{w}})$ whose parameters have direct measured counterparts, and the subset $\boldsymbol{q}'' = \left(T_\delta, \gamma_{\mathrm{N}}^{\mathrm{CN}}\right)$ whose parameters appear implicitly in the model outputs dependencies such that $\boldsymbol{q} = (\boldsymbol{q}', \boldsymbol{q}'')$. Similar subsets are defined for the observations set. The subset $\boldsymbol{y}'_{\mathrm{obs}} = \left(P_{\mathrm{d}}^{\mathrm{meas}}, P_{\mathrm{s}}^{\mathrm{meas}}, T_{\mathrm{w}}^{\mathrm{meas}}\right)$, and the subset $\boldsymbol{y}''_{\mathrm{obs}} = \left(\dot{s}^{\mathrm{meas}}, \rho_{\mathrm{CN}}^{\mathrm{meas}}\right)$ are defined such that $\boldsymbol{y}_{\mathrm{obs}} = \left(\boldsymbol{y}'_{\mathrm{obs}}, \boldsymbol{y}''_{\mathrm{obs}}\right)$.

To solve Eq. (10), we need to prescribe a likelihood function $\mathcal{P}(\boldsymbol{y}_{\mathrm{obs}}|\boldsymbol{q})$ and a prior distribution $\mathcal{P}(\boldsymbol{q})$. The integral under the denominator in Eq. (10) is a normalization constant that extends to the space of $\boldsymbol{q}$, denoted here with the Greek letter Ω. In practical terms, such quantity is very hard to calculate because the likelihood (or the prior) can have extremely complex structure, with multiple compact modes, arbitrarily positioned in the (presumably high-dimensional) parameter space $\boldsymbol{q}$. In this regard, normalization-insensitive sampling techniques that rely on ratios of the unnormalized posterior distribution are desired. In this work, we use the Metropolis-Hastings (MH) algorithm [35], adapting the proposal covariance matrix using previously sampled points in a burn-in stage [36]. The scaling factor is selected to ensure an acceptance rate varying between 20 and 50% following Roberts et al. [37], and a sufficiently fast decorrelation of the chain. The starting point for the MCMC algorithm is also important. In this context, we consider the computation of the Maximum A Posteriori (MAP) point, $\boldsymbol{q}_{\mathrm{MAP}}$, expressed as

$$\boldsymbol{q}_{\mathrm{MAP}} = \arg\max_{\boldsymbol{q}}\ \mathcal{P}(\boldsymbol{q}|\boldsymbol{y}_{\mathrm{obs}}). \tag{11}$$

The MAP is estimated by solving Eq. (11) with a dedicated optimization procedure. To calculate the MAP, we rely on the Nelder-Mead algorithm which is robust enough as it does not make use of gradients [38].

The definition of the likelihood function encapsulates the forward model given that the parameters to be inferred have an implicit relation with the simulated observations. In Sec. 2.2 we referenced the model used to simulate the reacting boundary layer encountered in the experiments. Specifically, we can predict recession rates and CN densities which we can then compare to the observations. As already mentioned, without further modeling assumptions, we would have to infer 14 parameters. Further reasonable physical assumptions often adopted in the literature allow us to reduce the problem to a 5-dimensional inference where the most influential parameter is our quantity of interest $\gamma_{\mathrm{N}}^{\mathrm{CN}}$. Having our different sets of measurements and parameters defined, for each experimental condition we propose a general likelihood of the form

$$\mathcal{P}(\boldsymbol{y}_{\mathrm{obs}}|\boldsymbol{q}(\boldsymbol{\xi})) \propto \prod_{i=1}^{N'} \exp\left[-\frac{|y'_{\mathrm{obs},i} - q'_i(\xi'_i)|^2}{2\sigma^2_{y'_{\mathrm{obs},i}}}\right] \times \prod_{j=1}^{N''} \exp\left[-\frac{|y''_{\mathrm{obs},j} - Y_j(\boldsymbol{\xi})|^2}{2\sigma^2_{y''_{\mathrm{obs},j}}}\right], \tag{12}$$

where $q'_i, y'_{\mathrm{obs},i}$ represent the ith elements of the $\boldsymbol{q}', \boldsymbol{y}'_{\mathrm{obs}}$ sets, while $y''_{\mathrm{obs},j}$ is the jth element of the $\boldsymbol{y}''_{\mathrm{obs}}$ set. The terms N' and N'' refer to the number of elements in the prime $\boldsymbol{q}', \boldsymbol{y}'_{\mathrm{obs}}$ sets, and the observations double prime $\boldsymbol{y}''_{\mathrm{obs}}$ set, respectively. The dependency of the quantities q'_i with ξ'_i has been made explicit for clarity. In this case, ξ'_i denotes the canonical variables associated to the variables in $\boldsymbol{q}'$. As we recall from Sec. 3.1.1, the surrogates for recession rate and CN density $\boldsymbol{Y} = \left(10^{Y_{\dot{s}}}, 10^{Y_{\rho_{\mathrm{CN}}}}\right)$ are built on their logarithms to ensure the positivity of the approximation. The term $Y_j(\boldsymbol{\xi})$ is the jth element of the surrogates $\boldsymbol{Y}$ set already converted to natural scale. The standard deviations of the elements in both sets of measurements are expressed as $\sigma_{y'_{\mathrm{obs}},i}$ and $\sigma_{y''_{\mathrm{obs}},j}$.

As can be appreciated, in this likelihood, the measurement noise is assumed to follow independent Gaussian distributions with standard deviations σ. It is worth mentioning than in the first formulation of the dependencies of $\dot{s}$ and ρ_{CN} (Eqs (1),(2)) we have an explicit relation with the velocity components u_δ, v_δ. In the formulation of Eq. (12), the set $\boldsymbol{q}$ does not contain the velocity components but the dynamic pressure P_{d}. Even though we carry out the inference on the variable P_{d} instead of the velocity components, the relationship between them is computed externally and the velocity components are fed to the model to output $\dot{s}$ and ρ_{CN}. It is simpler to keep the original inputs to the solver which would allow us to use this framework as it is to assess possible discrepancies due to the assumptions embedded in the freestream computations, thereby having to include the velocities in the inference problem in the future.

Besides the likelihood function, we need to define prior distributions for all the parameters in $\boldsymbol{q}$. In the available literature for tests in the VKI Plasmatron and stagnation line plasma flows [14, 15, 39, 40], we can only establish some bounds a priori. In a maximum entropy set-up [41] with this a priori information, the resulting prior distributions are uniform over the prescribed range. The priors of $P_{\mathrm{d}}, P_{\mathrm{s}}$ and T_{w} are not going to be very relevant as we have direct measured counterparts for these parameters which will dominate in the final posterior. In this regard, we are not concerned with imposing a tight prior for these parameters when compared to the literature. We have to be more careful with T_δ and $\gamma_{\mathrm{N}}^{\mathrm{CN}}$. Even though the influence of the uncertainty of T_δ on $\dot{s}$ and ρ_{CN} is very small compared to $\gamma_{\mathrm{N}}^{\mathrm{CN}}$'s, we have to take into account that when performing an inference from $\dot{s}$ and ρ_{CN} jointly, we might run into inconsistencies among measurements, and T_δ could become important for the model to attain predictability for these cases as the second most influential parameter. For this reason, the priors for T_δ and $\gamma_{\mathrm{N}}^{\mathrm{CN}}$ are chosen conservatively wide. Table 4 shows the precise chosen prior distributions.

Table 4: Prior distributions for the inference parameters.

P_δ [Pa]	T_δ [K]	P_{d} [Pa]	T_{w} [K]	$\gamma_{\mathrm{N}}^{\mathrm{CN}}$
$\mathcal{U}[1200, 1700]$	$\mathcal{U}[9000, 13000]$	$\mathcal{U}[200, 360]$	$\mathcal{U}[2000, 4000]$	$\log \mathcal{U}[-4, 0]$

4. Inference results and discussion

We apply the developed methodology to the real experimental cases depicted in Sec. 2.1. The different cases comprise a set of experimental conditions with high heating and high surface temperatures.

Our inference analyses are carried out from different sources of information to potentially unveil some inconsistency issues with the model chosen and/or the measurements. The latter could be due to a bad reconstruction of the corresponding physical quantities from the raw data. Helber et al. [12] used the experimental data for two different tasks. They used recession rates to rebuild nitridation reaction efficiencies, and CN densities for validation of their rebuilding methodology. Recession rates are well understood and the transition from raw data to the physical quantity itself is rather straightforward. On the other hand, CN densities are the result of an elaborated rebuilding procedure with intermediate steps and modeling choices [42]. Unless a very careful uncertainty analysis was carried out upstream, from the raw data to the reduced model parameters of the spectrograph and on to the gas temperatures and CN densities, we cannot be confident in the bounds given for the CN densities or even the nominal values reported. Therefore, it is not fair for the model in question to be validated against not reliable experimental data. Cross-validating this way sources of information is useful for detecting inconsistencies stemming from inappropriate experimental data treatment and/or modeling choices. The key for this task is that nitridation influences both recession rates and CN densities and we can then compare their information on $\gamma_{\mathrm{N}}^{\mathrm{CN}}$ in an objective Bayesian inference scenario.

The next sections contain results and discussions on the inferences from different measurements on a one by one basis and also when combined all together in a single analysis. We recall that each experimental condition is treated separately and nitridation reaction efficiencies are computed for each case independently. Conversely, for the calibration of an Arrhenius law, the measurements from all cases are combined together.

4.1. Inference from recession rates

For the case of using only recession rates, pressures and wall temperatures, the likelihood formulated reads

$$\mathcal{P}(\dot{s}^{\mathrm{meas}}|\boldsymbol{q}(\boldsymbol{\xi})) \propto \prod_{i=1}^{N'} \exp\left[-\frac{|y'_{\mathrm{obs},i} - q'_i(\xi'_i)|^2}{2\sigma^2_{y'_{\mathrm{obs},i}}}\right] \times \exp\left[-\frac{|\dot{s}^{\mathrm{meas}} - 10^{Y_{\dot{s}}(\boldsymbol{\xi})}|^2}{2\sigma^2_{\dot{s}^{\mathrm{meas}}}}\right]. \tag{13}$$

Results are depicted in Fig. 5 where we can see that the marginal posterior distributions obtained for $\gamma_{\mathrm{N}}^{\mathrm{CN}}$ are well defined with a very reduced support. If we take a look at the experimental conditions, we would expect to see a tendency where $\gamma_{\mathrm{N}}^{\mathrm{CN}}$ increases as a function of the temperature at the wall, which is what is seen in these results (Fig. 6). Compared to the deterministic rebuilding performed by Helber et al., our results show agreement and consistency. This is due to the strong dependency of recession rates with nitridation reaction efficiencies and their quasi-linear relationship as seen in Fig. 3. We can also notice in Fig. 6 that the distributions of the measured wall temperatures are recovered after the model calibrations.

4.2. Inference from CN densities

If the chosen model can explain the experiments and the treatment of the raw experimental data is fully consistent with the workings of the experimental apparatus, one can expect the inference from different sources of information to give us consistent answers. In this regard, we explore the possibility of learning nitridation efficiencies from CN densities estimated from spectra measurements of the CN violet system. This measurement is plagued with assumptions about the nature of the CN radiative signature in these experiments. The fact that recession rates give us enough information about nitridation helps us assess the quality and assumptions on the spectra measurements. In the case of the inference from ρ_{CN}, the likelihood considered in this case reads

$$\mathcal{P}(\rho_{\mathrm{CN}}^{\mathrm{meas}}|\boldsymbol{q}(\boldsymbol{\xi})) \propto \prod_{i=1}^{N'} \exp\left[-\frac{|y'_{\mathrm{obs},i} - q'_i(\xi'_i)|^2}{2\sigma^2_{y'_{\mathrm{obs},i}}}\right] \times \exp\left[-\frac{|\rho_{\mathrm{CN}}^{\mathrm{meas}} - 10^{Y_{\rho_{\mathrm{CN}}}(\boldsymbol{\xi})}|^2}{2\sigma^2_{\rho_{\mathrm{CN}}^{\mathrm{meas}}}}\right]. \tag{14}$$

Fig. 7 shows the inference performed from CN densities, pressures and wall temperatures. The results are visibly different from Fig. 5 but the tendency of $\gamma_{\mathrm{N}}^{\mathrm{CN}}$ increasing with wall temperatures is also observed (Fig. 8), even though G6 seems to infer a quite higher $\gamma_{\mathrm{N}}^{\mathrm{CN}}$ than that from recession rates in order to match a ρ_{CN} that is larger than any of

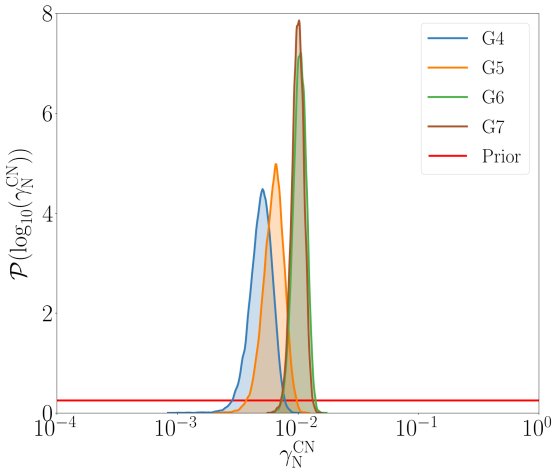

Figure 5: Posterior marginal distributions of γ_N^{CN} from recession rates.

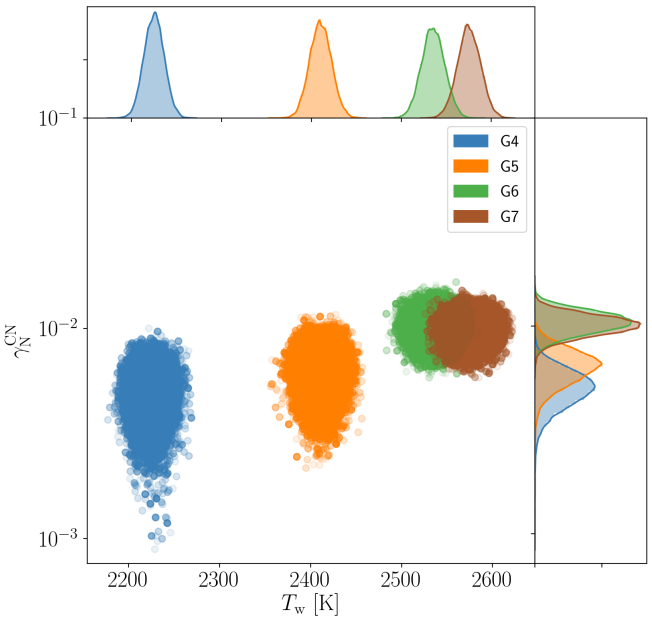

Figure 6: Joint posterior distribution of γ_N^{CN} and T_w from recession rates.

the other cases. We can notice as well that the support is larger compared to the support from recession rates in Fig. 5, meaning that CN density is a less precise measurement and also more sensitive to other parameters than recession rates. We can also see that there are two orders of magnitude of difference between the calibrated γ_N^{CN} for G4 and G6, while for recession rates results were more clustered around 10^{-2}. Overall, there is less information content in this set of measurements than the previous inference with s^{meas}.

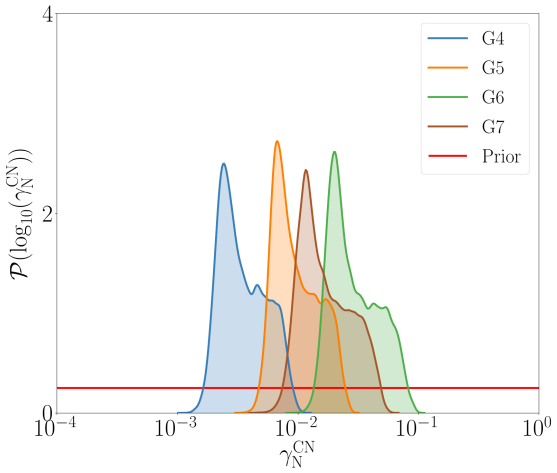

Figure 7: Posterior marginal distributions of γ_N^{CN} from CN densities.

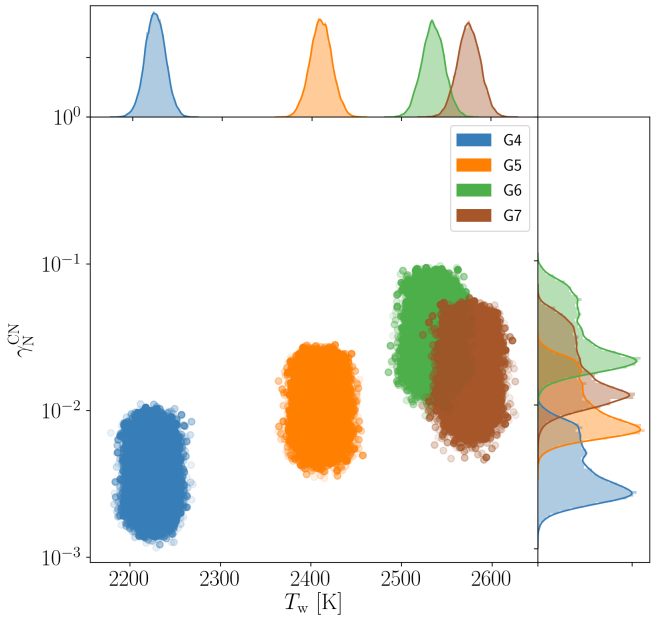

Figure 8: Joint posterior distribution of γ_N^{CN} and T_w from CN densities.

4.3. Inference from all available measurements

We could expect to learn better γ_N^{CN} if we use all sources of available information. This would be true if we assume that the model error is zero and that the raw data is correctly transformed into meaningful physical quantities. If somehow the model chosen to simulate our experiments is inadequate and there are some missing modeled components, we can probably expect to see a depart of the calibrated distributions obtained independently from each other. In turn, this tension among measurements under the chosen model will find a trade-off distribution when all measurements are used together in the inference but the predictive capabilities might be lost. We would also expect to see the marginal

posteriors of γ_N^{CN} from $\dot{s}^{meas}$ and ρ_{CN}^{meas} to share supports with each other. We can expect this overlapping fraction of the γ_N^{CN} posterior marginals to explain all measurements with a reduced support and information gain on the calibrated γ_N^{CN}. In this regard, the likelihood now includes all measurements following Eq. (12).

We can see in Fig. 9 the different inferences that we carried out when using each piece of information independently and jointly. Overall, we can see that the calibrations seem consistent. The support of the distributions obtained with all measurements is contained in within the support of each of the parts', and one can see some information gain (reduced support compared to either of the parts'). Good agreement seems to be found, although we can clearly see that as the wall temperature increases, there seems to be an over prediction of ρ_{CN} that is not fully consistent with the measurements of recession rates. This is reflected on the calibration of γ_N^{CN} as both measurements are directly and greatly affected by it. If we pay attention to case G6 (lower left), we can see that the overlap of support is very small and the distribution that contains the information of both measurements does not share most of its support with the calibration obtained by using only CN densities. It is clear that, in this case, the results represent a trade-off between the two measurements and this case must be studied further.

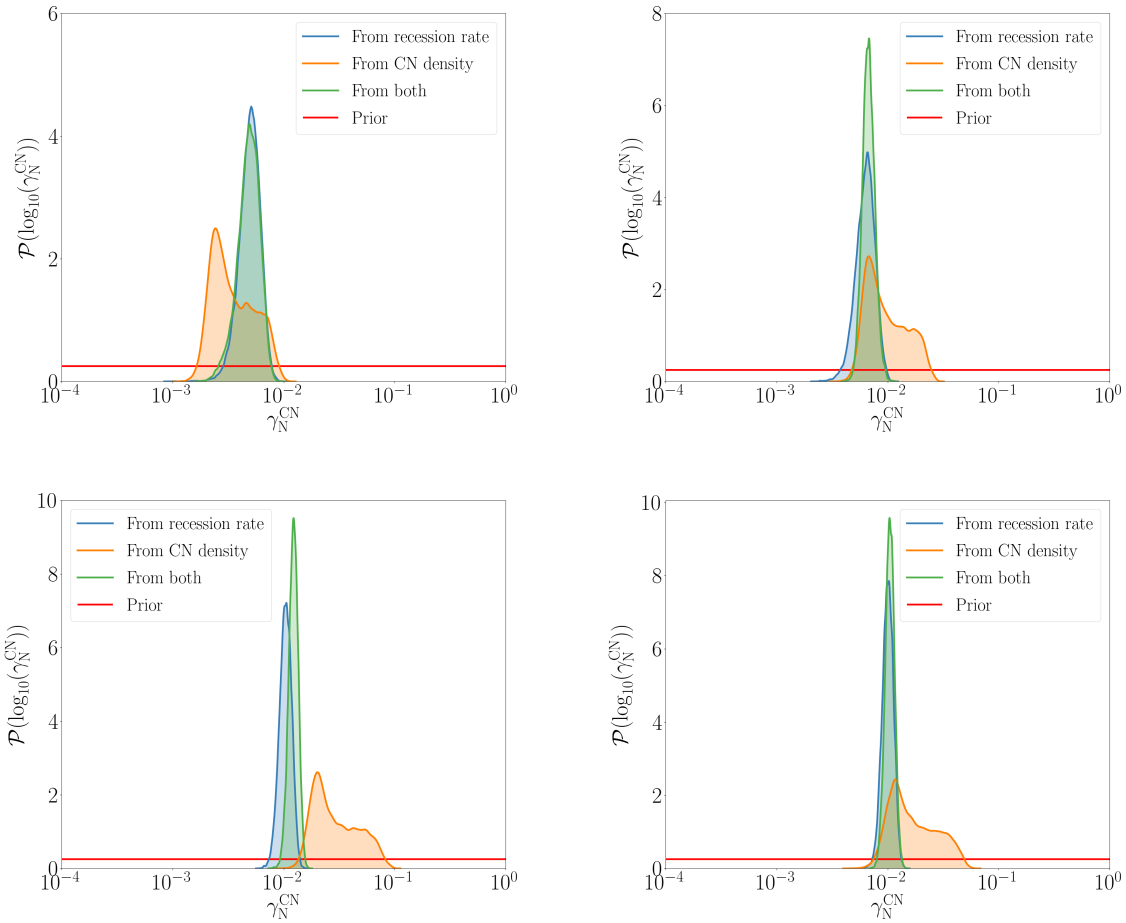

Figure 9: Posterior marginal distributions of γ_N^{CN} from recession rates, CN densities and both measurements for G4 (upper left), G5 (upper right), G6 (lower left) and G7 (lower right).

The inconsistencies with the measurements of G6 are likely to signal an issue with the measurements. The fact that things look good for all cases but G6 makes it unlikely for the chosen physico-chemical model to only fail at the conditions under which G6 was recorded, given that the testing conditions were steadily changed from one case to the next, always under the same static pressure. The testing conditions reach top values for G7, for which the inferences

do not present any inconsistencies. For this reason, we are led to consider this issue to be related to the measurements. Based on the work of Helber et al., no dedicated uncertainty propagation was carried out on the spectra measurement chain. This is particularly important given the intertwined and complex rebuilding to get from the integrated line-of-sight spectrum to local CN densities. We therefore base our attempt at explaining these results on the inadequacy of the uncertainty levels given by Helber et al. on the CN densities.

4.4. Inference with experimental uncertainty unknown

In this section, we include the uncertainty on $\rho_{\mathrm{CN}}^{\mathrm{meas}}$ as an additional parameter in the inference with all available measurements. We are interested in retrieving the values of $\sigma_{\rho_{\mathrm{CN}}^{\mathrm{meas}}}$ that would make the cases (specially G6) consistent across all measurements. Introducing an additional parameter in our inferences implies defining a prior distribution for such parameter and its role in the likelihood function. The latter issue is straightforward as the parameter introduced is a standard deviation which does not need to pass through any physical model or alter our likelihood formulation a priori.

We need to specify an objective prior for the standard deviation of a Gaussian distribution. For this, we prescribe a Jeffrey's prior [43] for $\sigma_{\rho_{\mathrm{CN}}^{\mathrm{meas}}}$ for each experimental case. The family of Jeffrey's priors are able to objectively capture our ignorance regarding parameter scaling which is what the standard deviation of a Gaussian distribution represents. The $\sigma_{\rho_{\mathrm{CN}}^{\mathrm{meas}}}$ prior for each experimental case is defined as follows

$$\mathcal{P}(\sigma_{\rho_{\mathrm{CN}}^{\mathrm{meas}}}) = \begin{cases} \dfrac{1}{\sigma_{\rho_{\mathrm{CN}}^{\mathrm{meas}}}} & \sigma_{\rho_{\mathrm{CN}}^{\mathrm{meas}}} \geq \sigma^{*}_{\rho_{\mathrm{CN}}^{\mathrm{meas}}}, \\ 0 & \text{otherwise.} \end{cases} \tag{15}$$

with $\sigma^{*}_{\rho_{\mathrm{CN}}^{\mathrm{meas}}}$ being the originally prescribed $\sigma_{\rho_{\mathrm{CN}}^{\mathrm{meas}}}$ by Helber et al. and depicted in Table 2. We are implicitly assuming that the actual uncertainty on the CN density experimental estimation is larger than what was originally computed, given the assumptions that go into it and not taken into account in the uncertainty computation.

The problem is now reduced to jointly infer $\boldsymbol{q}$ and $\sigma_{\rho_{\mathrm{CN}}^{\mathrm{meas}}}$ from all the available observations $\boldsymbol{y}_{\mathrm{obs}}$ for each experimental case. We proceed by using the full likelihood depicted in Eq. (12) together with the priors defined in Table 4 and Eq. (15). We want to analyse the results and, particularly, the marginal posteriors for $\sigma_{\rho_{\mathrm{CN}}^{\mathrm{meas}}}$ for each experimental case. We also recall from Table 2 that the value of $\sigma^{*}_{\rho_{\mathrm{CN}}^{\mathrm{meas}}}$ is dependent on each experimental case.

Fig. 10 shows the calibrated $\sigma_{\rho_{\mathrm{CN}}^{\mathrm{meas}}}$ for each case, as well as the transformed distribution for the logarithmic increment of $\sigma_{\rho_{\mathrm{CN}}^{\mathrm{meas}}}$ with respect to each case's $\sigma^{*}_{\rho_{\mathrm{CN}}^{\mathrm{meas}}}$. On the left plot of Fig. 10, we can see the different marginal posteriors for which their lower bounds coincide with their respective $\sigma^{*}_{\rho_{\mathrm{CN}}^{\mathrm{meas}}}$ which are dependent on each case (vertical lines), reason why they appear slightly shifted from each other. Overall, we retrieve the same kind of posteriors for all cases but G6, as expected. On the right plot of Fig. 10, while all the other cases' posteriors still support their respective $\sigma^{*}_{\rho_{\mathrm{CN}}^{\mathrm{meas}}}$ values (zero), G6 practically gives no chance to its initially prescribed standard deviation in order to be able to support the experimental data with the chosen model.

A minimum of a 10% increment on G6's $\sigma^{*}_{\rho_{\mathrm{CN}}^{\mathrm{meas}}}$ could already be enough to attain consistency and produce compatible results, although the optimal for G6 would be between one and ten times its $\sigma^{*}_{\rho_{\mathrm{CN}}^{\mathrm{meas}}}$ (100% and 1000% increment, respectively). A 10% increment is certainly a possibility. Twice the prescribed value of G6's $\sigma^{*}_{\rho_{\mathrm{CN}}^{\mathrm{meas}}}$ would not be a large stretch either, given the complexity of the densities rebuilding from the measured spectrum and all the parameters uncertainties that should be involved and are not yet. Even though from this procedure we have no way to actually prove that this is the reason why we observe inconsistencies in the inferences under G6 conditions, we can already prescribe the repetition of measurements and an adequate treatment of the raw data and associated uncertainties. In any case, this analysis can already rule out the possibility of learning from G6's $\rho_{\mathrm{CN}}^{\mathrm{meas}}$ to obtain a useful calibrated model given that the data cannot be fully trusted.

We also show in Fig. 11 the resulting posterior marginals for $\gamma_{\mathrm{N}}^{\mathrm{CN}}$ with $\sigma_{\rho_{\mathrm{CN}}^{\mathrm{meas}}}$ unknown. We can appreciate how we retrieve consistent posteriors across the different measurements. It is also important to notice that as we let $\sigma_{\rho_{\mathrm{CN}}^{\mathrm{meas}}}$ be calibrated, it will, in general, be larger than each $\sigma^{*}_{\rho_{\mathrm{CN}}^{\mathrm{meas}}}$ thus, in the inference, the recession rate $\dot{s}^{\mathrm{meas}}$ is the measurement driving the calibration of $\gamma_{\mathrm{N}}^{\mathrm{CN}}$. As the certainty in the measurement of $\rho_{\mathrm{CN}}^{\mathrm{meas}}$ decreases (larger values of $\sigma_{\rho_{\mathrm{CN}}^{\mathrm{meas}}}$), the posterior marginals of $\gamma_{\mathrm{N}}^{\mathrm{CN}}$ when using all available measurements are exactly the posterior marginals when using only $\dot{s}^{\mathrm{meas}}$.

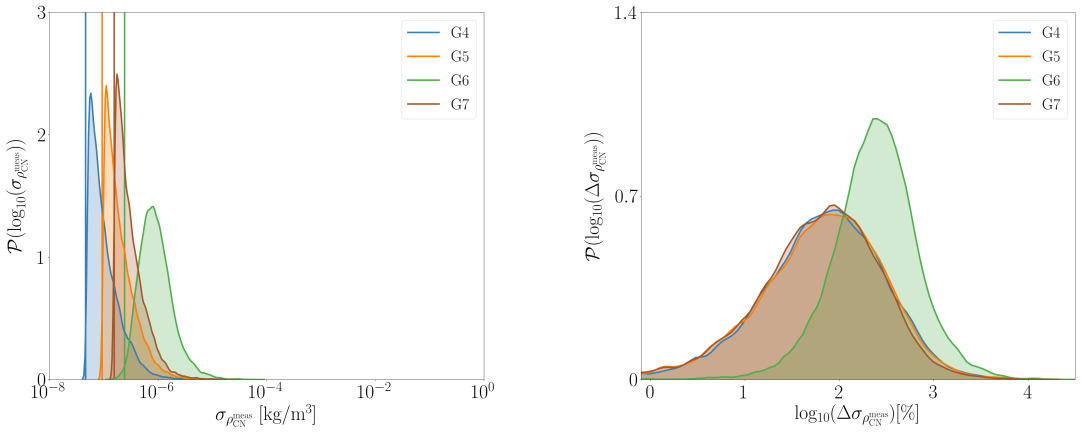

Figure 10: Left: posterior marginal distributions of $\sigma_{\rho_{CN}^{meas}}$. The vertical lines signal $\sigma^*_{\rho_{CN}^{meas}}$ for each case. Right: Their transformed logarithmic increment distributions with respect to the given values of $\sigma^*_{\rho_{CN}^{meas}}$ for each case.

The new parametrization of this inference problem is not free of caveats. As we let $\sigma_{\rho_{CN}^{meas}}$ vary freely without any upper bound, the resulting distributions for the measurement error of ρ_{CN}^{meas} can lead to possible negative values which is not physical. For this reason, we also consider a log-normal statistical model [44] for the measurement error of ρ_{CN}^{meas} for which the resulting possible values are always kept positive. We propose the same Jeffrey's prior for the log-normal standard deviation but in this case, the values $\sigma^*_{\rho_{CN}^{meas}}$ are taken as the logarithm of the $\sigma_{\rho_{CN}^{meas}}$ originally prescribed by Helber et al. (see Table 2). The likelihood proposed in this case is structured as follows

$$\begin{aligned}\mathcal{P}(\boldsymbol{y}_{obs}|\boldsymbol{q}(\boldsymbol{\xi})) \propto \prod_{i=1}^{N'} \exp\left[-\frac{|y'_{obs,i} - q'_i(\xi'_i)|^2}{2\sigma^2_{y'_{obs,i}}}\right] \exp\left[-\frac{|\dot{s}^{meas} - 10^{Y_{\dot{s}}(\boldsymbol{\xi})}|^2}{2\sigma^2_{\dot{s}^{meas}}}\right] \times \\ \times \frac{1}{10^{Y_{\rho_{CN}}(\boldsymbol{\xi})}\sqrt{2\pi\sigma^2_{\rho_{CN}^{meas}}}} \exp\left[-\frac{|\log_{10}\rho_{CN}^{meas} - Y_{\rho_{CN}}(\boldsymbol{\xi})|^2}{2\sigma^2_{\rho_{CN}^{meas}}}\right].\end{aligned} \tag{16}$$

The results of the inference for this error model are shown in Fig. 12. Here, $\sigma_{\rho_{CN}^{meas}}$ is taken in decades. We can already observe the same tendency as with the previous error model. All cases have now an equivalent $\sigma^*_{\rho_{CN}^{meas}}$ in the log-normal distribution around 0.1 decades which makes the posterior marginals start from roughly the same values in all cases. The posterior marginals for γ_N^{CN} do not present visible changes for the inference performed with all measurements (Fig. 13). On the other hand, the resulting posterior marginals for γ_N^{CN} when considering only ρ_{CN}^{meas} are quite different. This is due to the appearance of an additional term in the likelihood function. For a log-normal likelihood we have to take into account an additional term as the inverse of the density ρ_{CN}, which is transformed as the negative value of the log of ρ_{CN} when considering the log-likelihood function for the MCMC sampling. This additional term favours smaller ρ_{CN} over larger ones, giving as a consequence preference to smaller γ_N^{CN} values in the calibration as seen in Fig. 13. Overall, we can draw the same conclusions regarding the data from G6.

4.5. Calibration of an Arrhenius law for γ_N^{CN}

The scrutiny of the different sources of information for γ_N^{CN} allows us to build a calibrated Arrhenius model with the remaining consistent experimental data. In theory, we could propose any mathematical form for the relationship between γ_N^{CN} and surface temperatures T_w. An Arrhenius law of the form

$$\gamma_N^{CN} = A \exp\left(\frac{-T_a}{T_w}\right), \tag{17}$$

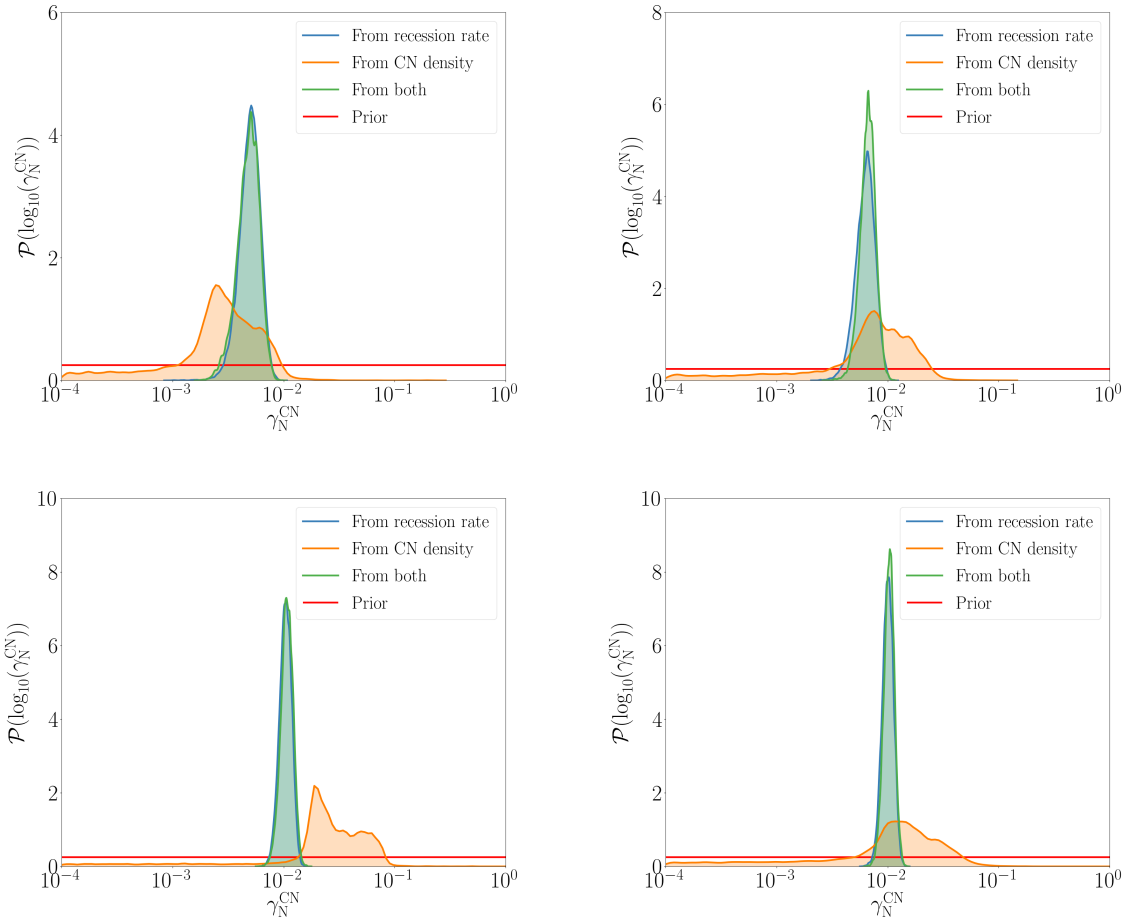

Figure 11: Posterior marginal distributions of γ_N^{CN} from recession rates, CN densities and both measurements for G4 (upper left), G5 (upper right), G6 (lower left) and G7 (lower right) with $\sigma_{\rho_{CN}}$ unknown.

with the pre-exponential factor A, and the activation energy (given in temperature units) T_a, is a familiar model in the state-of-the-art nitridation modeling [12, 45]. Apart from the possibility of producing direct comparisons between the models derived in this work and in the relevant literature, an Arrhenius law model also captures some of the underlying macroscopic physics through its parameters [46].

For this analysis, we aim at calibrating the pre-exponential factor A and the activation energy T_a which are the same for all cases. Along with the Arrhenius parameters, we need to add all the nuisance parameters to the calibrations. In this case, each nuisance parameter is represented as a different variable for each experimental case. The compact notation is as follows. For each case (i) in $\mathbf{G} = (G_4, G_5, G_6, G_7)$, we define the set of parameters to be inferred as $\boldsymbol{q}^{(i)} = (\boldsymbol{q}^{'(i)}, \boldsymbol{q}^{''(i)})$, and the set of observations from which we infer $\boldsymbol{y}_{obs}^{(i)} = (\boldsymbol{y}_{obs}^{'(i)}, \boldsymbol{y}_{obs}^{''(i)})$. While the sets of observations remain the same as in the previous sections, the set of parameters to be inferred is now changed to $\boldsymbol{q}^{(i)} = (P_\delta^{(i)}, T_\delta^{(i)}, P_d^{(i)}, T_w^{(i)}, A, T_a)$, where A and T_a do not depend on the experimental conditions and they are the same for all cases. The split for the set $\boldsymbol{q}^{(i)}$ is now $\boldsymbol{q}^{'(i)} = (P_\delta^{(i)}, P_d^{(i)}, T_w^{(i)})$, and $\boldsymbol{q}^{''(i)} = (T_\delta^{(i)}, A, T_a)$.

For this new inference problem, we need to define a new parametrization in the form of likelihood and prior distributions. We propose the following likelihood

$$\mathcal{P}(\boldsymbol{y}_{obs}|\boldsymbol{q}(\boldsymbol{\xi})) \doteq \prod_{i\in\mathbf{G}} \mathcal{P}(\boldsymbol{y}_{obs}^{(i)}|\boldsymbol{q}^{(i)}(\boldsymbol{\xi})), \tag{18}$$

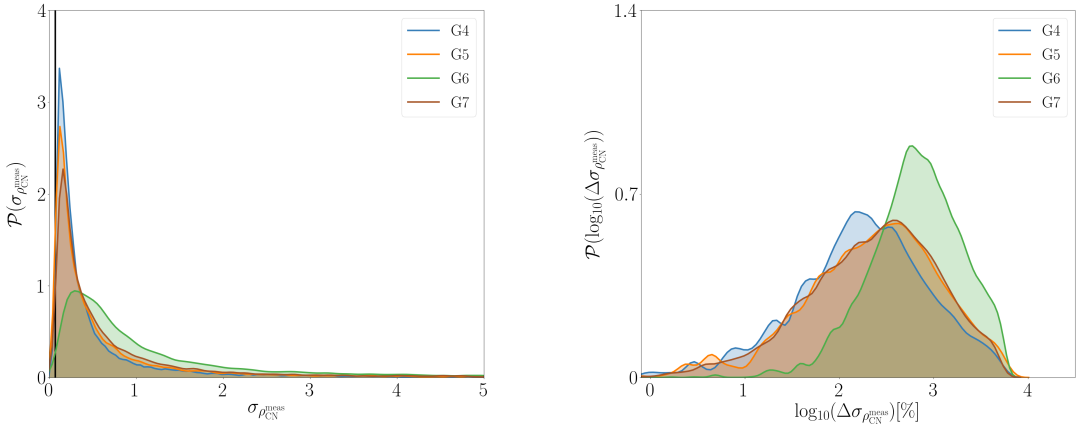

Figure 12: Posterior marginal distributions of $\sigma_{\rho_{CN}}$ and their transformed logarithmic increment distributions with respect to the equivalent $\sigma^*_{\rho_{CN}}$ from all measurements.

with

$$\mathcal{P}(\boldsymbol{y}^{(i)}_{obs}|\boldsymbol{q}^{(i)}(\boldsymbol{\xi})) \propto \prod_{j=1}^{N'} \exp\left[-\frac{|y^{'(i)}_{obs,j} - q^{'(i)}_j(\xi'_j)|^2}{2\sigma^2_{y^{'(i)}_{obs,j}}}\right] \times \prod_{k=1}^{N''} \exp\left[-\frac{|y^{''(i)}_{obs,k} - Y_k(\boldsymbol{\xi})|^2}{2\sigma^2_{y^{''(i)}_{obs,k}}}\right]. \tag{19}$$

We use this formulation to compare the results of the inferences when using only recession rates to the ones obtained when using all consistent data jointly. We recall that, in the case of conditions G6, only the measured recession rate is used.

We perform the different inferences with 18 parameters to be calibrated. The prior distribution is taken as independent priors on all parameters, already specified in Sec. 3.2. For A, we prescribe the same prior as for γ_N^{CN} as it is an equivalent parameter, in this case, $A \sim \log \mathcal{U}[-4, 0]$. The prior on T_a is chosen wide enough with the same lower bound as the prior on T_w, given that we expect the activation energy to be at least as low as the a priori possible lowest T_w. It is not easy to prescribe a good upper bound as there is not so much literature on this particular reaction parameter. We choose the upper bound conservatively large based on the results of Suzuki et al. [45] and Helber et al. [12], having $T_a \sim \mathcal{U}[2000, 10000]$.

The results of these inferences are shown in Fig. 14. The plot on the left is the calibrated Arrhenius law that results from using all available measurements except G6's ρ_{CN}^{meas}, while the right plot contains the calibrated Arrhenius law when using only recession rates from all cases. The up-close plots show the two dimensional joint probability density functions of γ_N^{CN} and T_w as the result of each individual inference for comparison with the Arrhenius bounds obtained. The calibrated laws are represented by their mean and 95% confidence interval bounds. We can see that there is a reduction of the law parameters uncertainty when using all available information compared to using just recession rates. From recession rates we can learn $A = 0.26^{+0.22}_{-0.22}$ and $T_a = 8027.4^{+1899.6}_{-3832.3}$ to that precision, while incorporating all measurements gives us different estimations $A = 0.28^{+0.22}_{-0.21}$ and $T_a = 8337.8^{+1608.2}_{-3308.3}$. The major uncertainty reduction is in the activation energy T_a and it mainly comes from the combined measurements of G5. We already saw a reduction of the γ_N^{CN} posterior marginal uncertainty for G5 when using all measurements. This is also the case for the Arrhenius parameters. For G4 and G7, we saw that the posterior marginals of γ_N^{CN} changed little or nothing when using recession rates or all measurements, while for G5 the combination of $\dot{s}^{meas}$ and ρ_{CN}^{meas} saw a more prominent reduction of the support than for any one measurement alone. The data used for G6 is the same in both cases as we cannot trust the CN density reported. Both results contain the fit produced by Helber et al. in their posterior. The major discrepancy is seen in the low temperature region for which our inferences do not use any experimental data, unlike Helber et al., who included in their fit some selected cases in the lower temperature region.

A more quantitative measure of the reduction of uncertainty observed when using all data versus using recession

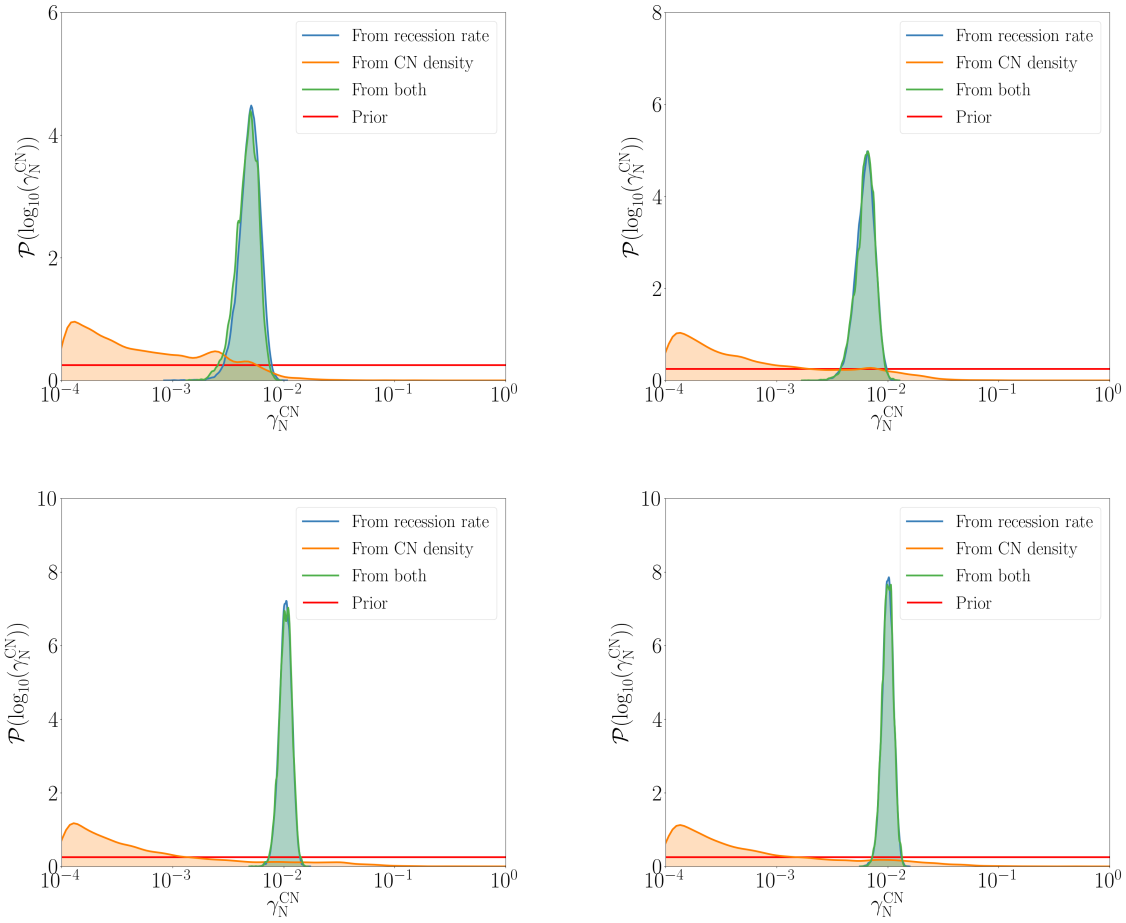

Figure 13: Posterior marginal distributions of γ_N^{CN} from recession rates, CN densities and both measurements for G4 (upper left), G5 (upper right), G6 (lower left) and G7 (lower right) with the log-normal $\sigma_{\rho CN}$ unknown.

rates can be seen in Fig. 15. It represents how much larger in relative percentage is the resulting standard deviation of the distribution of γ_N^{CN} predicted by the Arrhenius model calibrated using only recession rates compared to the one calibrated using all the trustworthy data. In Fig. 15, it can also be appreciated how for low surface temperatures the reduction of uncertainty in γ_N^{CN} is more prominent while both Arrhenius laws tend to equate their resulting γ_N^{CN} standard deviations for surface temperatures for which we have measurements (in the vicinity of $\sim$ 2,500 K).

The impact of the information brought by the experimental data to the Arrhenius law can be better appreciated in Fig. 16. The γ_N^{CN} distributions that result from the calibrated Arrhenius law with all measurements evolve from low to high surface temperatures. We can appreciate the most precise characterization for surface temperatures where we have experimental data.

It is interesting to show the results that are obtained if the measured CN density of case G6 is taken into account. Fig. 17 shows the obtained calibrated Arrhenius model, as well as a close-up plot of the two dimensional joint posteriors for the different cases. From the close-up plot, we can observe that the case G6 has more weight in the inverse problem, considerably deviating upward the general trend followed by the other cases captured in the Arrhenius laws of Fig. 14. Consequently, the resulting law is significantly modified for the upper and lower values of wall temperatures. The upper surface temperature region leaves completely out the estimation by Helber et al., while for lower surface temperatures, the calibrated law encompasses Helber et al.'s estimation at the very limit of the confidence interval. There is a substantial modification of the resulting uncertainty levels in the lower surface temperatures region

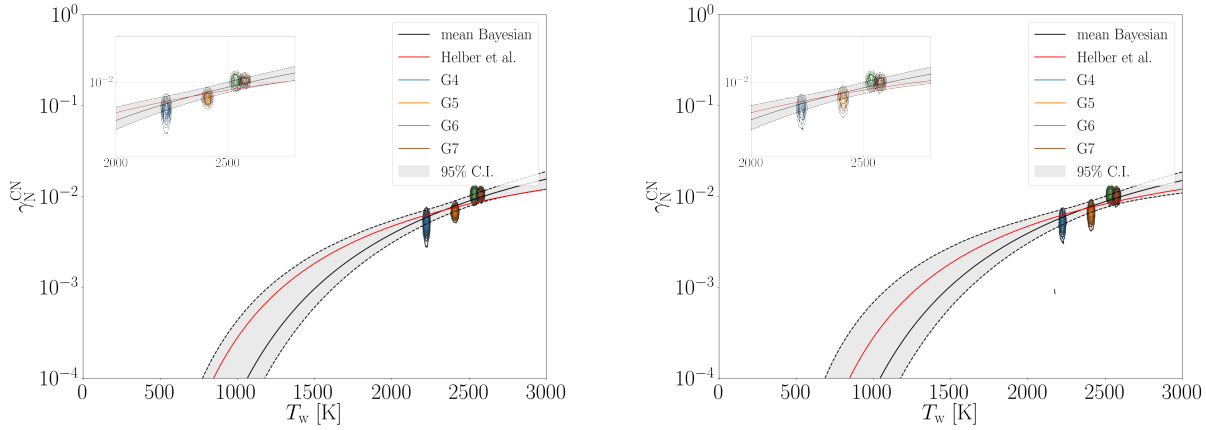

Figure 14: Calibrated Arrhenius laws from the data used in this work. Left: resulting law using all consistent measurements with specified bounds for the 95% C.I.: $0.28^{+0.22}_{-0.21}\exp\left(-\frac{8337.8^{+1608.2}_{-3308.3}}{T_w}\right)$. Right: resulting law using only recession rates: $0.26^{+0.22}_{-0.22}\exp\left(-\frac{8027.4^{+1899.6}_{-3832.3}}{T_w}\right)$.

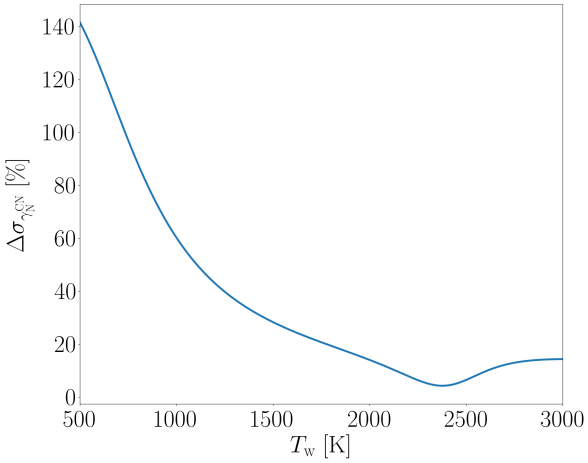

Figure 15: Relative differences on the obtained γ_N^{CN} standard deviations using both calibrated Arrhenius laws.

for which no additional experimental data are taken into account. In turn, this result falsely decreases the uncertainty levels in the range of lower surface temperatures.

5. Concluding remarks and outlook

The aim of this work is to infer nitridation reaction efficiencies from plasma wind tunnel experiments. We propose an a priori study of the chosen 1D chemical non-equilibrium stagnation line forward model to discard some experimental data that are not important to the phenomenon we want to study. To do so, we propagate a priori uncertainty levels on all the input and model parameters and derive variance-based sensitivity indices. This procedure shows that information of the boundary layer edge conditions does not play a role in the inference we want to carry out. Consequently, we can drop some experimental data that would otherwise complicate the inference by adding other models and computations to the likelihood estimation. This result also informs the experimental procedures about which data

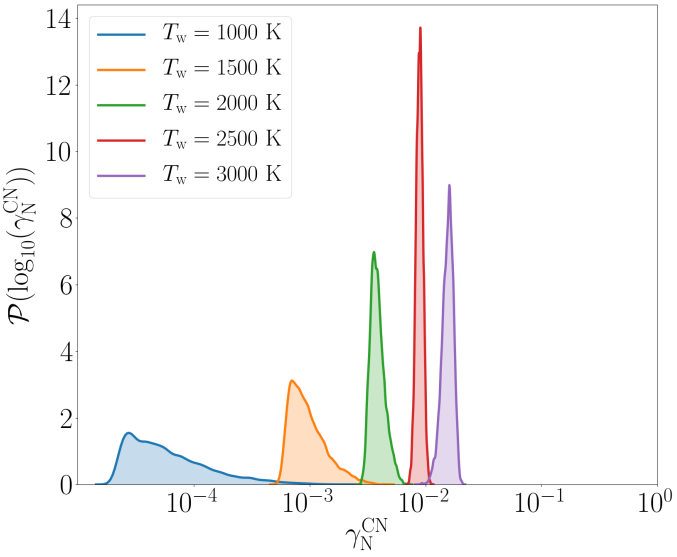

Figure 16: Posterior marginal distributions of γ_N^{CN} for a range of surface temperatures predicted by the Arrhenius law calibrated with all experimental data.

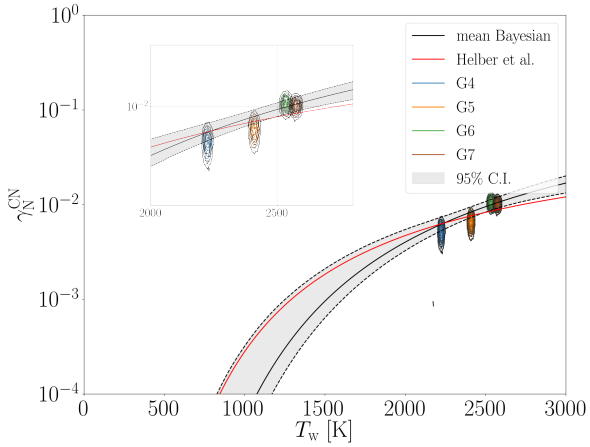

Figure 17: Calibrated Arrhenius law from all available measurements, including the measured CN density of case G6.

are informative for ablation processes, potentially allowing the simplification of future experimental campaigns. To carry out the a priori analysis, we propose to use Gaussian processes as surrogate models for the predicted quantities. The surrogate models are also used for the inference procedure.

The inference is splitted in terms of the experimental data used. We want to gauge the different levels of information that recession rates and CN densities bring to the inference of nitridation efficiencies. By comparing and combining them, we check for consistency issues in the experimental data and/or the model. Overall the calibrations seem consistent, the supports of the distributions obtained with all the measurements are generally contained in within the support of each of the parts and one can see some uncertainty reduction. We conclude that the spectrometer measurements for the case G6 present inconsistencies which are likely to stem from the lack of uncertainty treatment in the complex rebuilding chain from the line-of-sight spectra to local CN densities. The rationale behind this is the fact

that there is nothing special about conditions G6. The testing conditions were steadily changed from one case to the next, always under the same static pressure, reaching top values for G7, for which the inferences do not present any inconsistencies. We follow up the analysis by including in the inference the uncertainty on the measured CN densities. Apart from the initially adopted Gaussian measurement error model, we also adopt a log-normal error for the CN density measurements. For both cases the conclusion about G6 is the same. We recommend that the measurements are repeated and carefully analysed.

Gathering the consistent data from all the experimental conditions allows us to infer Arrhenius law parameters, relating the nitridation efficiencies to different wall temperatures. For this task, we compare the results when combining all consistent measurements and when using only recession rates. The results differ mainly on the uncertainty levels obtained for the activation energy. Most of the difference is due to the information given by the combination of recession rates and CN densities for the case G5.

The outcomes of this contribution direct our research efforts in this field towards two different aspects. The spectra measurements should be studied in depth and proper uncertainty propagation methods should be used to go from raw data, to the parameters of the reduced models of the apparatus and forward to flow temperatures and species concentrations. In doing so, the inference of physical model parameters with the derived measured quantities can improve and be more reliable when building new models. On the other hand, the model choice presented here is based on flow thermal equilibrium assumptions which may not hold for such low static pressures. The heterogeneous chemical mechanism is also ignoring the fact that nitrogen recombination might be important. The incorporation of a surface energy balance may additionally constrain the boundary layer edge energy flux, making it possible to even learn the edge temperature from these experimental data. All these modeling choices should be assessed and new experiments envisaged to test these models further.

Acknowledgements

This work is fully funded by the European Commission H2020 programme, through the UTOPIAE Marie Curie Innovative Training Network, H2020-MSCA-ITN-2016, Grant Agreement number 722734. The authors would also like to thank Dr. Alessandro Turchi and Dr. Bernd Helber for their useful insights, comments and guidance in understanding the data and use of the models.

References

[1] B. Laub, E. Venkatapathy, Thermal protection system technology and facility needs for demanding future planetary missions, in: Proceedings of international workshop on planetary probe atmospheric entry and descent trajectory analysis and science, 2004, pp. 239 – 247.

[2] G. Duffa, Ablative Thermal Protection Systems Modeling, AIAA Education Series, 2013.

[3] F. Panerai, J. Ferguson, J. Lachaud, A. Martin, M. Gasch, N. Mansour, Micro-tomography based analysis of thermal conductivity, diffusivity and oxidation behavior of rigid and flexible fibrous insulators (2017), International Journal of Heat and Mass Transfer 108 (2017) 801–811. doi:https://doi.org/10.1016/j.carbon.2017.09.081.

[4] H. W. Goldstein, The reaction of active nitrogen with graphite (1964), The Journal of Physical Chemistry 68 (1) (1964) 39–42. doi:10.1021/j100783a007.

[5] C. Park, D. Bogdanoff, Shock-tube measurements of nitridation coefficients of solid carbon (2006), Journal of Thermophysics and Heat Transfer 20.

[6] T. Suzuki, K. Fujita, K. Ando, T. Sakai, Experimental study of graphite ablation in nitrogen flow (2008), Journal of Thermophysics and Heat Transfer 22.

[7] L. Zhang, D. A. Pejaković, J. Marschall, M. Dougherty, D. G. Fletcher, Laboratory investigation of the active nitridation of graphite by atomic nitrogen (2012), Journal of Thermophysics and Heat Transfer 26 (1) (2012) 10–21. doi:10.2514/1.T3612.

[8] C. Park, D. W. Bogdanoff, Shock-tube measurement of nitridation coefficient of solid carbon (2006), Journal of Thermophysics and Heat Transfer 20 (3) (2006) 487–492. doi:10.2514/1.15743.

[9] V. J. Murray, T. K. Minton, Gas-surface interactions of atomic nitrogen with vitreous carbon (2019), Carbon 150 (2019) 85–92. doi:https://doi.org/10.1016/j.carbon.2019.04.117.

[10] V. J. Murray, P. Recio, A. Caracciolo, C. Miossec, N. Balucani, P. Casavecchia, T. K. Minton, Oxidation and nitridation of vitreous carbon at high temperatures (2020), Carbon 167 (2020) 388–402. doi:https://doi.org/10.1016/j.carbon.2020.05.076.

[11] R. R. Upadhyay, K. Miki, O. A. Ezekoye, J. Marschall, Uncertainty quantification of a graphite nitridation experiment using a bayesian approach (2011), Experimental Thermal and Fluid Science 35 (8) (2011) 1588–1599. doi:https://doi.org/10.1016/j.expthermflusci.2011.07.010.

[12] B. Helber, A. Turchi, T. E. Magin, Determination of active nitridation reaction efficiency of graphite in inductively coupled plasma flows (2017), Carbon 125 (2017) 582–594.

[13] A. del Val, Bayesian calibration and assessment of gas-surface interaction models and experiments in atmospheric entry plasmas, Ph.D. thesis, IPP/VKI (2021).

[14] B. Helber, Material Response Characterization of Low-density Ablators in Atmospheric Entry Plasmas, Ph.D. thesis, Vrije Universiteit Brussel,von Karman Institute for Fluid Dynamics (2016).
[15] F. Panerai, Aerothermochemistry Characterization of Thermal Protection Systems, Ph.D. thesis, Università degli Studi di Perugia,von Karman Institute for Fluid Dynamics (2012).
[16] A. Viladegut, Assessment of Gas-Surface Interaction Modelling for Lifting Body Re-Entry Flight Design, Ph.D. thesis, Universitat Politecnica de Catalunya,von Karman Institute for Fluid Dynamics (2017).
[17] A. Klomfass, S. Muller, A quasi-onedimensional approach for hypersonic stagnation-point flows, Tech. rep., RWTH Aachen (1996).
[18] A. Turchi, Multi-scale Models and Computational Methods for Aerothermodynamics Applications, Ph.D. thesis, École Central Paris, von Karman Institute for Fluid Dynamics (2014).
[19] K. Kitamura, E. Shima, Towards shock-stable and accurate hypersonic heating computations: A new pressure flux for ausm-family schemes (2013), Journal of Computational Physics 245 (2013) 62–83. doi:https://doi.org/10.1016/j.jcp.2013.02.046.
[20] J. B. Scoggins, V. Leroy, G. Bellas-Chatzigeorgis, B. Dias, T. E. Magin, Mutation++: MUlticomponent Thermodynamic And Transport properties for IONized gases in C++ (in the arxiv https://arxiv.org/abs/2002.01783, 2020). arXiv:2002.01783.
[21] G. Bellas, Development of Advanced Gas-surface Interaction Models for Chemically Reacting Flows for Re-entry Conditions, Ph.D. thesis, Politecnico di Milano, von Karman Institute for Fluid Dynamics (2018).
[22] Y.-K. Chen, F. Milos, Navier-stokes solutions with finite rate ablation for planetary mission earth reentries (2005), Journal of Spacecraft and Rockets 42.
[23] D. Bianchi, F. Nasuti, E. Martelli, Navier-Stokes simulations of hypersonic flows with coupled graphite ablation (2010), Journal of Spacecraft and Rockets 47 (2010) 554–562.
[24] A. Turchi, D. Bianchi, F. Nasuti, M. Onofri, A numerical approach for the study of the gas-surface interaction in carbon-phenolic solid rocket nozzles (2013), Aerospace Science and Technology 27 (2013) 25–31.
[25] B. Dias, Thermal ablation and radiation modeling of meteor phenomena, Ph.D. thesis, Université Catolique de Louvain/VKI (2020).
[26] T. Magin, A Model for Inductive Plasma Wind Tunnels, Ph.D. thesis, ULB/VKI (2004).
[27] G. Degrez, D. V. Abeele, P. Barbante, B. Bottin, Numerical simulation of inductively coupled plasma flows under chemical non-equilibrium (2004), International Journal of Numerical Methods for Heat & Fluid Flow 14 (4) (2004) 538–558. doi:10.1108/09615530410532286.
URL https://doi.org/10.1108/09615530410532286
[28] D. V. Abeele, G. Degrez, Efficient Computational Model for Inductive Plasma Flows (2000), AIAA Journal 38 (2) (2000) 234–242. doi:10.2514/2.977.
[29] A. Lani, N. Villedieu, K. Bensassi, L. Koloszar, M. Vymazal, S. M. Yalim, M. Panesi, COOLFluiD: an open computational platform for multi-physics simulation and research, in: 21st AIAA Computational Fluid Dynamics Conference, 2013-2589.
[30] G. Degrez, P. Barbante, M. de la Llave, T. E. Magin, O. Chazot, Determination of the catalytic properties of TPS materials in the VKI ICP facilities, in: European Congress on Computational Methods in Applied Sciences and Engineering ECCOMAS Computational Fluid Dynamics Conference 2001 Swansea, Wales, UK, 4-7 September 2001.
[31] I. Sakraker, Aerothermodynamics of Pre-Flight and In-Flight Testing Methodologies for Atmospheric Entry Probes, Ph.D. thesis, ULg/VKI (2016).
[32] M. Barker, On the use of very small pitot-tubes for measuring wind velocity (1922), Proceedings of the Royal Society A: Mathematical, Physical and Engineering Sciences 101.
[33] P. Chen, N. Zabaras, I. Bilionis, Uncertainty propagation using infinite mixture of gaussian processes and variational bayesian inference (2015), Journal of Computational Physics 284 (2015) 291–333.
[34] I. Sobol, Global sensitivity indices for the investigation of nonlinear mathematical models (2005), Mathematical Modeling 17 (2005) 43–52.
[35] H. Haario, E. Saksman, J. Tamminen, An adaptive metropolis algorithm (2001), Bernoulli 7 (2001) 223–242.
[36] Statistical and Computational Inverse Problems, Springer-Verlag, New York, 2005.
[37] G. O. Roberts, J. S. Rosenthal, Optimal Scaling for Various Metropolis–Hastings Algorithms (2001), Statistical Science 16 (2001) 351–367.
[38] J. A. Nelder, R. Mead, A simplex method for function minimization, in: Comput. J., Vol. 7 (4), 1965, p. 308–313.
[39] A. Viladegut, Assessment of Gas-Surface Interaction Modelling for Lifting Body Re-Entry Flight Design, Ph.D. thesis, VKI/UPC (2017).
[40] G. Bellas, Development of advanced gas-surface interaction models for chemically reacting flows for re-entry conditions, Ph.D. thesis, VKI/Politecnico di Milano (2018).
[41] D. S. Sivia, J. Skilling, Data Analysis - A Bayesian Tutorial, 2nd Edition, Oxford Science Publications, Oxford University Press, 2006.
[42] D. L. Quang, Spectroscopic Measurements of Sub- and Supersonic Plasma Flows for the Investigation of Atmospheric Re-Entry Shock Layer Radiation, Ph.D. thesis, Université Blaise Pascal,von Karman Institute for Fluid Dynamics (2014).
[43] C. P. Robert, N. Chopin, J. Rousseau, Rejoinder: Harold jeffreys's theory of probability revisited (2009), Statistical Science 24 (2) (2009) 191–194.
[44] E. Limpert, W. A. Stahel, M. Abbt, Log-normal Distributions across the Sciences: Keys and Clues (2001), BioScience 51 (5) (2001) 341–352.
[45] T. Suzuki, K. Fujita, T. Sakai, Graphite nitridation in lower surface temperature regime (2010), Journal of Thermophysics and Heat Transfer 24 (1) (2010) 212–215. doi:10.2514/1.43265.
[46] W. G. Vicenti, C. H. Kruger, Introduction to Physical Gas Dynamics, Krieger Pub Co., 1975.